MONITORING HANGING GLACIER DYNAMICS FROM SAR IMAGES USING CORNER REFLECTORS AND FIELD MEASUREMENTS IN THE MONT-BLANC MASSIF

Suvrat Kaushik[1,2]*, Silvan Leinss[2], Ludovic Ravanel[1], Emmanuel Trouve[2], Yajing Yan[2], Florence Magnin[1]

[1] EDYTEM, CNRS, Université Savoie Mont Blanc, Le Bourget du Lac, France
[2] LISTIC, Université Savoie Mont Blanc, Annecy, France

Corresponding author: suvrat.kaushik@univ-smb.fr

KEY WORDS: Hanging glacier, SAR images, corner reflectors, dGNSS survey, Mont-Blanc massif

ABSTRACT:

This paper focuses on the monitoring of a small hanging glacier with Synthetic Aperture Radar (SAR) images using a combination of artificial Corner Reflectors (CRs) and dGNSS field measurements. First, to test the performance of the CRs in high-resolution X-band and medium-resolution C-band images acquired by PAZ and Sentinel-1 satellites respectively, a series of tests was performed with two CRs installed in the Chamonix valley. After the confirmation of good visibility in the valley datasets from both satellites, four CRs were installed in summer 2021 on a steep ($\approx 52°$ average slope) hanging glacier on the North face of Aiguille du Midi (3842 m a.s.l., Mont-Blanc massif). After the successful installation on the hanging glacier, all CRs were visible in both sets of images (PAZ and Sentinel-1). Using the CRs as a reference, glacier displacements were estimated in SAR images using complex cross-correlation, and validated by using ground measurements (dGNSS) and theoretical relationships between ice thickness and surface velocity. We observed average summer velocities of ≈ 0.05 m/day at the front of the glacier from field measurements and ≈ 0.04 m/day from SAR displacement estimates. The study shows the potential and limitations of using CRs as a tool for monitoring glaciers in complex topographies.

1. INTRODUCTION

Over the recent years, hanging glaciers (HGs) have been a source of destabilizations because of the complex topography they are generally associated with (Cuffey and Paterson, 2010). Destabilizations of HGs are marked by a periodic or occasional release of ice by calving (Pralong and Funk, 2006). The break off ice can trigger ice falls, rock falls or even ice avalanches; although not very frequently, it can pose a significant threat to human life, infrastructure, and settlements (Jóhannesson and Arnalds, 2001). Historically, a few catastrophic events, like the snow/ice avalanche in Santa Valley in 1962 and the Ancash avalanche triggered by an earthquake in 1970; Peru have been recorded worldwide (Patzelt et al., 1983). In the Alpes, the most catastrophic event occurred in 1965, when a large section of the Allalin glacier, located in the rear part of the Saas valley (Switzerland), broke and killed 88 workers of a hydroelectric project the Saas valley (Raymond et al., 2003). The most devastating type of catastrophe arising from the instabilities of HGs is the ice avalanche, which increases in size gradually as it accumulates debris, snow, and water along with their movement downwards (Margreth et al., 2017). Previously, a few authors have discussed the potential reasons for these instabilities arising in HGs, and various theories in this regard have been put forward. (Faillettaz et al., 2011) suggested that the stability of HGs decreases as the temperature at the interface between the glacier base and the bedrock (basal temperature) reaches the melting point. This can lead to a situation where the glacier can become destabilized and slide downslope (Cuffey and Paterson, 2010). Thus, understanding how cold glaciers are warming in the future is key to understand the dynamics of these glaciers. There is also widespread evidence about the warming of cold glaciers from historical records resulting in many cold glaciers becoming temperate before the end of the century (Hoelzle et al., 2011). Additionally, permafrost degradation resulting in the melting of subsurface ice also tends to lower the stability of the mountain slopes, stimulating catastrophic downslope mass movements (Magnin et al., 2020). Landscapes that are de-glaciating are hence more prone to chain reactions and the resulting far-reaching catastrophic hazards like, high-elevated bedrock failures triggering debris, mudflows, or avalanches that can potentially devastate valley floors over large distances (Haeberli et al., 2017).

Assessment of potential glacial hazards related to environmental changes resulting from climate change in mountain areas most importantly requires systematic inventories to better understand the spatial and temporal distribution of the glacial systems and landforms (Smith et al., 2011). These inventories are important to point out possible areas or sites at risk where more detailed investigations are necessary. However, performing direct measurements on an unstable, steep, and heavily crevassed glacier is very challenging (Helfricht et al., 2015). Modelling the physical processes of HGs is also arduous because of their complex geometry, effects of ice advection on the temperature field, effect of meltwater percolation and refreezing of snow and ice, and influence of firn on the rheology (Maggioni et al., 2018). As a result, measurements for HGs are often sparse. Modern remote sensing-based techniques offer numerous possibilities to examine interactions and processes occurring over vast areas in glacial environments, which are often difficult to access (Gao and Liu, 2001). Glacier hazard studies based on remote sensing

* Corresponding author

techniques have been successfully conducted globally for all significant mountain regions, like the Alpes, Himalayas, and the Andes (Quincey et al., 2005). Studies using satellite-based observations may not always provide an in-depth understanding of the glacier dynamics as field surveys. However, studies have shown immense potential for an initial assessment of regional hazards to identify potential sources of hazard from mapped glacial terrain surfaces like rock and debris, ice, snow, water, lake (Huggel et al., 2004). Radar images hold an advantage over optical images because of their all-weather all-day capabilities. Many studies of ice flow estimations using radar images are available for large Alpine glaciers or polar regions, but these studies become more complex and rare for small glaciers, especially those on steep slopes (Quincey et al., 2005).

To monitor small HGs in the Mont-Blanc massif (western European Alps) utilizing Synthetic Aperture Radar (SAR) images, artificial Corner Reflectors (CRs) present great potential. CRs behave like point targets, providing a strong backscattering response in SAR images (Jauvin et al., 2019). They are characterized by a much higher reflectivity than the surrounding scatterers because of a high Radar Cross-Section (RCS) and signal-to-noise ratio (SNR) (Groot and Otten, 1994). This makes the CRs a perfect tool for monitoring areas characterized by complex topography and where field measurements are challenging. Keeping this in perspective, we performed a series of experiments to test the visibility of CRs in high-resolution X-band PAZ and medium-resolution C-band Sentinel-1 images in the Chamonix valley. After successful visibility tests on the valley floor, we installed four CRs to monitor a small HG on the North face of Aiguile du Midi (AdM). Four Differential GPS (dGNSS) readings were taken from June till October, 2021 to measure displacements on field for validation of results from SAR images. The movement of CRs could be simultaneously tracked and monitored by using the CRs as a reference in PAZ images. The study provides details of a first attempt at monitoring such small steep HGs using radar images.

This paper is organized as follows: Section 2 gives a brief description of the study site and the datasets considered for these experiments. Section 3 presents the methodology behind the CRs and displacement measurements using various techniques. Section 4 discusses the results about the visibility of CRs and the displacement estimations for the HG considered for the study. The paper ends with a brief conclusion of theses experiments, including the limitations and future opportunities.

2. TEST SITE AND DATASETS

2.1 Test site

The test site chosen for the study is a HG on the North face of AdM in the Mont-Blanc massif (Figure 1). The HG is 255 m long, and the maximum width is 160 m. The thickness at the glacier front as observed from photographic observations is ≈ 60 m. The mean slope of the glacier is 52°, while the mean aspect is 350° (North orientation). The elevation at the glacier front is 3384 m a.s.l. and at the top is 3677 m a.s.l. Events of ice/snow release from the glacier front are common with the most recent event reported on June 14, 2021 (one day after the CR installation), when a large serac fell on the right bank, triggering a snow slab avalanche.

Initial tests for visibility and signal quality assessment of the CRs were performed in a gently sloping (≈ 6°) open field in the Chamonix valley [45°54′29.90″ N, 6°51′03.20″ E, 1077 m a.s.l.] on 15/01/2021 (Figure 2). After successful tests and the confirmation of good visibility of CRs in both the sets of images, we installed two CRs on the stable area (rock) near the AdM station on June 9, 2021 [45°52′49.94″ N, 6°53′22.25″ E, 3656 m a.s.l.] (descending) (Figure 3-a) and [45°52′49.32″ N, 6°53′25.87″ E, 3652 m] (ascending), and two CRs at the front of a HG on the North face of AdM on June 13, 2021 [45°52′54.34″ N, 6°53′16.00″ E, 3464 m] (ascending) (Figure 3-b) and [45°52′54.43″ N, 6°53′15.84″ E, 3460 m] (descending).

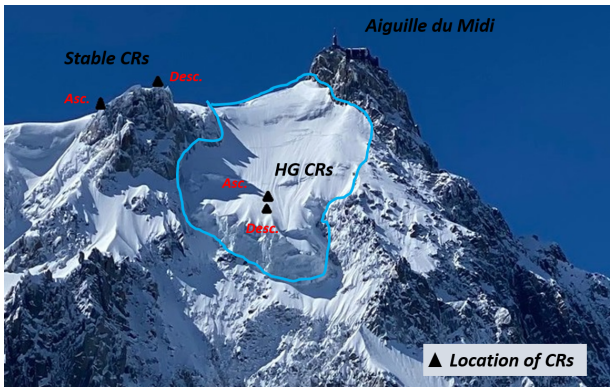

Figure 1. Study site and the locations of the CRs.

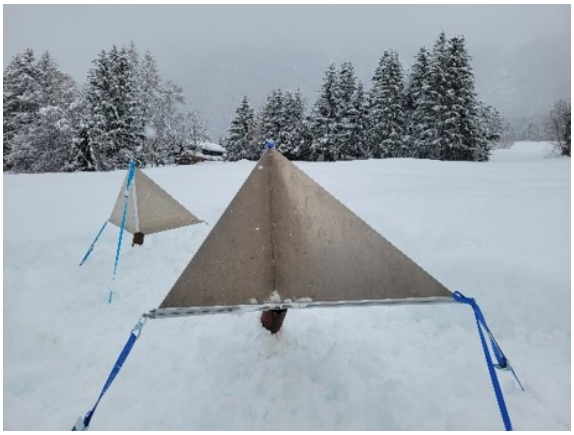

Figure 2. Corner reflectors installed in Chamonix valley, January-June 2021. Picture taken on 15/01/2021 (the first date of CR installation).

2.2 Datasets

The datasets used in this study are summarized in Table 1.

Datasets used	Resolution (m)	Acquisition time	Inc. angle (°)
Pleiades DEM	4	25/09/2019	-
PAZ (asc.)	2.1 × 2.1	11 days	54.3
PAZ (des.)	2.1 × 2.1	11 days	37.8
Sentinel-1 (asc.)	5 × 15	6 days	44.2
Sentinel-1 (des.)	5 × 15	6 days	40.3

Table 1. Datasets used in the study.

a. Descending CR installed on the stable area (09/06/2021)

b. Ascending CR installed on the HG (13/06/2021)

Figure 3. CRs installed near Aiguille du Midi for HG monitoring.

For the analysis with SAR images, time series of high-resolution X-band PAZ images and medium resolution C-band Sentinel-1 images were used. All images were downloaded in the Single Look Complex (SLC) file format. PAZ images are available at 11-day time interval, but not systematically acquired, while the Sentinel-1 images are available every 6 days. The acquisition geometry of both satellites is almost similar (as also described in table 1). Hence, a compromise in the orientation angles of the CRs for the good visibility in both datasets could be achieved as described in Section 3.1

3. METHODOLOGY

To work with data from two different satellites, that have different orbit and sensor characteristics, it was imperative to perform visibility tests to select the orientation of the CRs and to evaluate the effect of snowfall events on their backscattered signal. For this, we performed multiple tests by installing the CRs in Chamonix valley and assessing the quality of the signal return in both PAZ and Sentinel-1 datasets. After this, we installed the CRs on the HG, and glacier displacement was estimated using SAR images, dGNSS measurements and empirical relationships.

3.1 Orientation of CRs

The strength of the signal return from CRs as observed in SAR images depends on many factors like shape, size and orientation angles (Sarabandi and Chiu, 1996). For this study, a set of 4 triangular trihedral shaped CRs was used. The RCS peak of such CRs is calculated using the equation as follows:

$$\sigma_{RCS} = \frac{\pi L^4}{3\lambda^2} \tag{1}$$

where L is the length of the sides of the CR and λ is the radar wavelength.

Further, the signal strength also depends on the azimuth (α_{CR}) and elevation angles (ψ) of the CRs, which in turn depends on the satellite azimuth (α_s) and incidence angles (θ_s). A trihedral CR can be considered as an object whose Radar Cross Section (RCS) depends on its open face. The direction of the maximum RCS (peak return) is defined as normal to the open face of the CR. Thus, the radar wave is normal to the open face when the angle between the radar Line of Sight (LOS) and one of the side plates is equal to $tan^{-1}(1/\sqrt{2})$, so around 35.26°. To use the same CR for two different satellites with different incidence angles (*cf.* table 1), a compromise between the two satellite parameters had to be done. We considered a compromised $\theta_s = 40°$ for both ascending and descending data and azimuth angles of 9° (descending) and 351° (ascending). Based on this, ψ can be calculated using the following equation:

$$\psi + 35.26 + \theta_s = 90 \tag{2}$$

So $\psi = 15°$

Utilizing these orientation settings, two CRs were initially installed in the Chamonix valley from January 15 till June 10 for visibility tests (Figure 2).

3.2 Displacement measurements: theoretical, field based and SAR based

The displacements/velocities of glaciers can be estimated from various techniques, which have all proven their advantages based on the objectives and location of the study. Here we discuss three commonly used techniques in the following sub-sections:

3.2.1 Theoretical displacement Theoretically ice thickness or velocities can be estimated using the equation of laminar flow (Cuffey and Paterson, 2010):

$$H = \sqrt[4]{\frac{1.5U_s}{Af^3(\Phi g \sin\alpha)^3}} \tag{3}$$

where, H is the ice thickness in meters. U_s is the surface velocity, α is the estimated slope derived from the Pleiades Digital Elevation Model (DEM), Φ is the density (which can be estimated or considered as a constant value of 900 kg m^{-2}), g is the acceleration due to gravity (9.8 ms^{-1}), f is the shape factor, the value of which ranges from 0.6 - 1 and A is the creep parameter, which is assigned a constant value of 3.24 * 10^{-24} Pa^{-3} s^{-1}.

3.2.2 Field measurements The location of the descending CR was measured on four different dates throughout the summer by performing a dGNSS survey. The measurements were taken on 13/06, 09/07, 17/09 and 29/10 in 2021. dGNSS measurements provide x,y,z coordinates for each date with an accuracy of a few centimeters. Raw data collected from the study site, requires further post processing, which can be performed using the Trimble Business Center software bundled along with the dGNSS. The post processing of the raw data involves utilizing the base stations available closest to the study site to correct the readings taken during field observations.

3.2.3 SAR based displacement estimation To measure the CRs displacement in image pairs, the so-called "phase correlation" method was used, which is a Fourier-based matching technique considered to be more accurate and robust than other correlation-based methods (Amitrano et al., 2019). Two PAZ descending images in which the HG CR was visible were utilized for the analysis. The reference image (19/06/2021) and the secondary image (02/08/2021) were processed using the following steps and displacement of the CRs was estimated at sub-pixel level. The methodology is decomposed of the following steps:

- extracting a square window in each (reference and secondary) image containing the CRs (a window patch size of 64 * 64 was used for the study),
- transforming the images from spatial to frequency domain by applying discrete Fast Fourier Transform (D-FFT),
- deapodizing/deweighting the images by applying a 2D hamming window to remove the effects of the hamming weights,
- multiplying the complex conjugate of the second image with the first element wise to calculate the cross-power spectrum,
- applying zero padding by inserting zeros at high frequencies to extend the cross-power spectrum, (a factor of 8 was utilized for applying the zero padding for this analysis)
- applying inverse Fourier transform to obtain the normalized cross-correlation,
- identifying the sub-pixel location of the cross-correlation peak by fitting a parabola function,
- subtracting global co-registration values (estimated from the orbits and the DEM) to obtain the final displacement.

4. RESULTS AND DISCUSSION

4.1 Visibility tests for the CRs in the Chamonix valley

Figure 4-a shows the effect of a snowfall (comparison before and after a snowfall event) on the signal strength from the CRs. Because of the wet snow which accumulates in the CR, the signal return from the CRs was completely lost. To mitigate the effects of snow (especially wet snow) filled in the CRs, the CRs were covered with a cover of 0.2 cm thickness. The effect of covering the CR with the cover can be seen from Figure 4-b. We observed a loss in the peak signal return of ≈ 1 dB before and after covering the CRs. But the signal strength was consistent and no loss in signal was observed after covering the CRs, even after snowfall events. The ideal Impulse Response Function (IRF) was also maintained for the entire time period of observation. This indicates the effectiveness of covering the CRs in areas of low to medium accumulation.

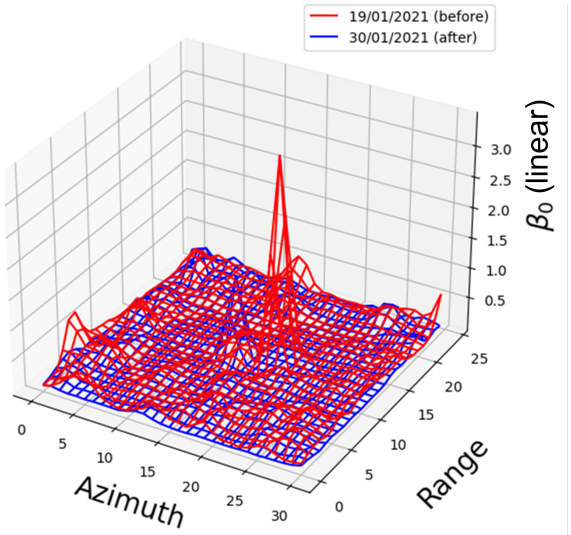

(a) CR signal return before and after a snowfall event.

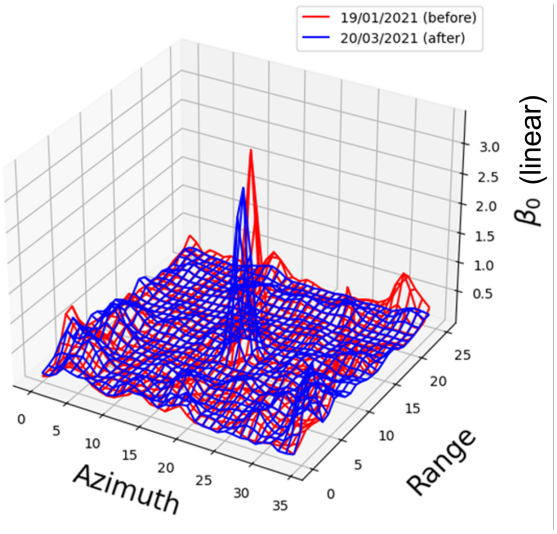

(b) CR signal return before and after covering the CR.

Figure 4. Tests in the Chamonix valley to check CR performance in Sentinel-1 images.

4.2 Visibility of CRs on the hanging glacier

As mentioned in Section 2, four CRs were installed for the observation of the steep North face of AdM. The visibility of the CRs was checked in both Sentinel-1 and PAZ images to confirm successful installation. Figure 5-a shows the visibility of the CRs in descending Sentinel-1 images (16/06/2021), while Figure 5-b shows the same for ascending Sentinel-1 images (17/06/2021). The two stable CRs were visible in all images of Sentinel-1 and PAZ acquired during the period of observation (from 15/06/2021 to 18/10/2021). However, the HG CR was visible clearly only on three dates in PAZ images acquired on 19/06/2021 (Figure 6-a), 30/06/2021 and 02/08/2021. The ascending HG CR was visible in PAZ images acquired on 15/06/2021 (Figure 6-b) and 26/06/2021. The ascending HG

This contribution has been peer-reviewed. The double-blind peer-review was conducted on the basis of the full paper.
https://doi.org/10.5194/isprs-annals-V-3-2022-325-2022 | © Author(s) 2022. CC BY 4.0 License.

CR was unfortunately not visible in any PAZ images after this date. For Sentinel-1 images all the CRs were visible in images acquired on 17/06/2021 and 18/06/2021 and then again on images taken on 23/06/2021 and 24/06/2021. The visibility of the HG glacier CRs was lost for all other dates except those mentioned above.

Figure 8 shows the annual evolution of the backscatter coefficient (σ_0) for the HG CRs (red profile), stable CRs (blue profile), the HG (black profile) and the entire scene average (grey profile) in Sentinel-1 ascending and descending images. Except for the images acquired just after the CR installation on the HG, no peaks are observed and the signal from both ascending and descending CRs almost merges with that from the HG. Hence it is impossible to distinguish the CRs from the glacier background. As for the stable CRs, we see a consistent sharp peak throughout the study period, indicating a good visibility for these CRs in Sentinel-1 images.

The lack of radar response of the HG ascending CR is probably due to an avalanche or crevasse fall since it was impossible to find it on the following field missions. For the HG descending CR, it could be attributed either to the degradation of the CR orientation settings or to the significant snowfall events completely covering and submerging the CRs inside several layers of more or less wet snow. The first hypothesis can be rejected since the initial orientation settings did not change and was verified every time the descending CR position was measured by GNSS. The second hypothesis is discussed further in Section 4.3.

From these results, it is clear that CRs could be successfully installed, and observed in extremely complex topographic environments and that the plastic cover is sufficient to avoid the presence of snow inside the CRs without significant signal loss. However, the maintenance of the CRs in these environments depends on many external factors beyond the human control.

4.3 Loss of radar cross section for CR buried in snow on steep slopes

In this section we investigate the effects of the snow covering the CRs on their signal response. The two main expected effects are:

- the misalignment due to the change of incidence angle caused by the refraction of microwaves on the snow-pack;
- the distortion of the wave fronts caused by heterogeneous snow-pack.

The loss of RCS with misalignment can be calculated for different shapes of CRs (Sarabandi and Chiu, 1996). Figure 7 shows that the trihedral corner reflectors (TCR) used for this experiment have the lowest sensitivity to misalignment compared to all other reflector shapes. For a misalignment of 25° either only in elevation or in horizontal direction (azimuth), a signal loss of not more than 5-6 dB is expected (light blue curve). According to the orbit geometry of the descending HG CR and the snow cover in the 40° steep north-facing slope of snow with an estimated density of $\rho = 0.3 g/cm^3$, the line-of-sight vector changes its direction due to refraction (n_{snow} = 1.24, (Mätzler, 1996)) by 17°. With such misalignment, the

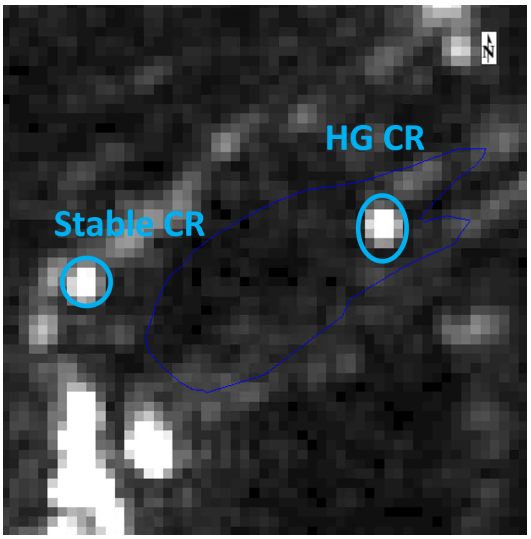

a. Sentinel-1 descending image (16/06/2021)

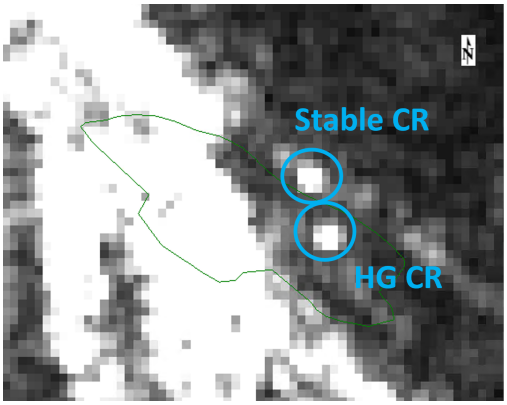

b. Sentinel-1 ascending image (17/06/2021)

Figure 5. Visibility of the CRs on the HG (blue and green polygons) in Sentinel-1 images in SAR range-azimuth geometry.

RCS loss would be only 2.3 dB, possibly 4-5 dB at the most unfortunate case of both, elevation and azimuth misalignment. Comparing this with the backscatter plots of the CRs and of the surrounding glacier (Figure 8) indicates that the CRs should still be visible in Sentinel 1 images for certain dates. Similarly the backscatter plots for PAZ ascending and descending images shows similar results to Sentinel 1 (Figure 9).

The distortion of the wave fronts caused by heterogeneous snow-pack is probably the most critical effect (*cf.* p. 350-356 in (Mätzler, 1987). When the snow density is homogeneous and the propagation delay due to thickness-variations of the snow cover is well below the wavelength, no phase distortions occur. This is the case for the cover of the upper stable CRs which most of the time was free of snow or covered by only a few cm of snow (sun and wind exposure removed most snow). With a deeper snow cover affecting the HG CRs in the accumulation area (exposed to spin-drift, i.e. snow trickling down the HG), the resulting phase variation is $\Delta_{phi} = 2\pi(n(\rho) - 1).L/\lambda$ where $n(\rho)$ is the density dependent refractive index and L the path length that microwaves travel through snow. For example, $n = 1.24$ ($\rho = 0.3 g/cm^3$), L = 1 m, λ = 5.5 cm (C-band), result in 4.3 wavelengths of signal delay by the snow-pack. A delay-variation of half

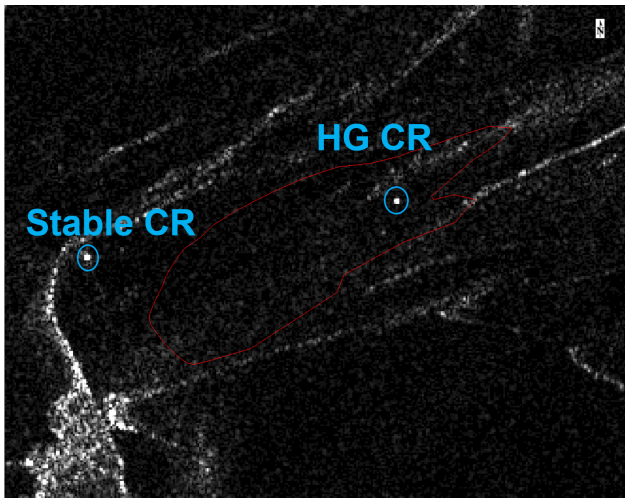

a. PAZ descending image (19/06/2021)

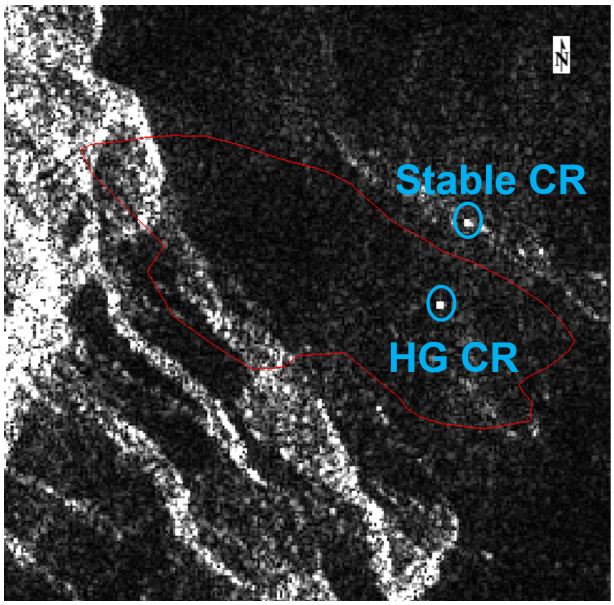

b. PAZ ascending image (15/06/2021)

Figure 6. Visibility of the CRs on the HG (red polygons) in PAZ images in SAR range-azimuth geometry.

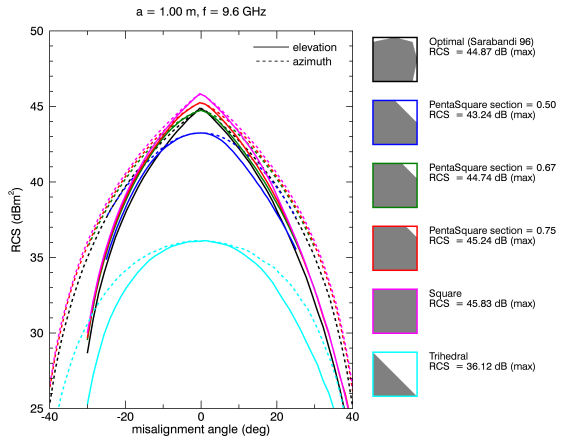

Figure 7. Loss of Radar Cross Section (RCS) due to misalignment for different shapes of CR.

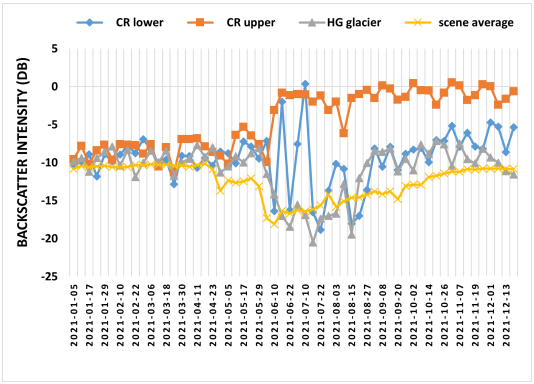

a. Descending (orbit: 139)

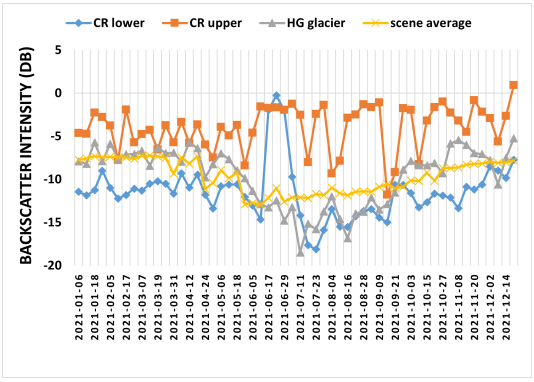

b. Ascending (orbit: 161)

Figure 8. Backscatter coeffcient time series for Sentinel-1 images.

a wavelength across the illuminated area of the CR already completely destroys the plane wave fronts making the CR invisible. For the given numbers, a delay of half a wavelength corresponds to a refractive index variation from 1.237 to 1.265 or 2%, corresponding to a density change of 11%. Considering the two-way propagation doubles the sensitivity, a density change of only 6% is sufficient to produce an incoherent back-scattering over the illuminated area of the corner reflector. The above equation can also be used to estimate the thickness variation of a snow cover on a CR which is sufficient to add a half-wavelength-delay to the wave fronts. For $n = 1.24$ ($\rho = 0.3 g/cm^3$), 6 cm of snow thickness variation can be sufficient to make the CR invisible at C-band. The effect is even more critical at X-band but less at L-band. (Eppler and Rabus, 2022) was able to detect a trihedral CR under 3 m of dry snow on a horizontal area at L-band but could not detect the CR in X-band.

4.4 Displacement measurements from different techniques

The thickness of the AdM HG as estimated from previous LiDAR and photogrametric surveys is ≈ 60 m at the glacier front. Considering this estimate, and utilizing the theoretical values previously mentioned in Section 3.2.1, from the equation of laminar flow, expected theoretical glacier velocities are in the range of 9-10 m/year at the glacier front. Furthermore results from the dGNSS survey show that the CRs moved by ≈ 6.82 m between 13/06/2021 and 29/10/2021 (138 summer days) (Table 2). The mean daily displacement was thus 0.049 m/day. The direction of the movement was 352° N, which also corresponds to the direction of the steepest slope

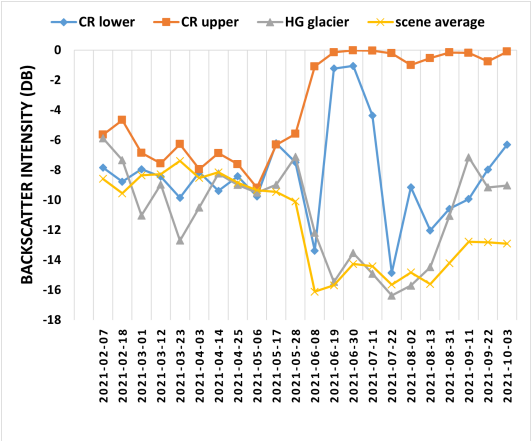

a. Descending

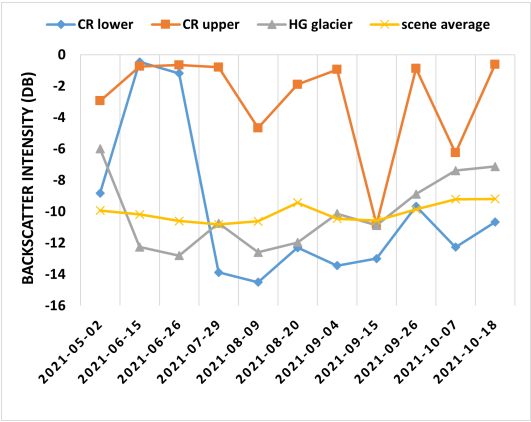

b. Ascending

Figure 9. Backscatter coefficient time series for PAZ images.

direction of the glacier. The maximum displacement was observed during the period from 13/06/2021 to 09/07/2021 as the observed average daily displacement was 0.067 m/day during this period.

For the analysis from SAR images, the correlation peak, Argmax($peak_{(x,y)}$) was found at (94.54, 1.91) (Figure 10). Considering that the initial images were up-scaled by a factor of 8 during the zero padding step, we divide the (x, y) values with 8 to get the shift in original pixel counts. So, the correlation peak in original pixel geometry is at (11.93, 0.23). Multiplying this by the spatial resolution of the PAZ data, we get offset values of (25.74, 0.53) m. This value also includes the global pixel offset between the two images, that needs to be subtracted from the correlation peak value. The global offset maps in range and azimuth directions were generated from the EFIDIR toolbox (Benoit et al., 2015). Looking at the global offset maps, the offset is $\approx (24, 0.1)$ m in range and azimuth directions. Subtracting this from the correlation offset we finally get offset values of (1.74, 0.43) m in range and azimuth directions. This value indicates the displacement between the two images (19/06/2021 and 02/08/2021). Thus, the HG velocity at the CR location, projected in the 2D range-azimuth image plane of PAZ SAR sensor, is about 0.04 m/day.

4.5 Uncertainity assessment

An assessment of the processing errors can be carried out using the stable CRs as reference. All available descending images for PAZ was processed to estimate displacements over

Date of image	Coordinates (dd)	Elev. (m a.s.l.)	Displ. (m)
13/06/2021	45.881187, 6.887975	3504.42	-
09/07/2021	45.887971, 6.881198	3503.25	1.76
17/09/2021	45.881218, 6.887961	3500.06	3.18
29/10/2021	45.881226, 6.887956	3498.37	1.88

Table 2. dGNSS survey readings.

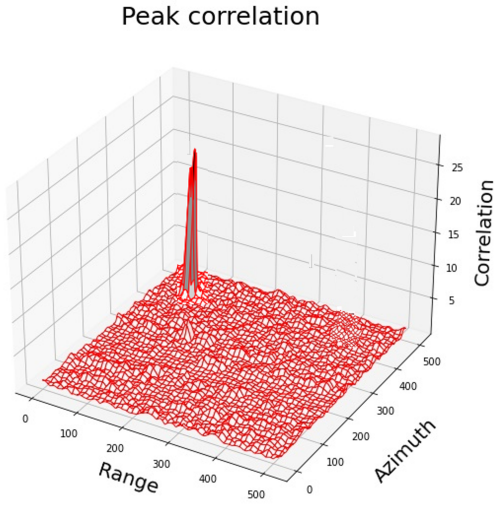

Figure 10. Correlation peak measured between 2 PAZ 64x64 pixel patches oversampled by a factor of 8 by zero padding.

the stable CR. Root Mean Square Error (RMSE) was calculated to average the displacement between all image pairs after subtracting the global offset from the displacement measurements. The RMSE for all descending PAZ image pairs was found to be 0.15 pixels in range and 0 pixels in azimuth ($\approx$ 0.3 m in range). Specifically for the two image pairs considered for the displacement estimation using cross correlation, the RMSE was found to be 0.11 pixels in range and 0 pixels in azimuth ($\approx$ 0.22 m), so about 0.004 m/day.

5. CONCLUSIONS

The present study illustrates the potential of using artificial CRs for glacier displacement tracking in extremely complex topographies. It also further emphasizes the advantages of using SAR data for continuous monitoring of glaciers. In the first part, we focused on analysing the response of the CR in PAZ and Sentinel-1 datasets. To mitigate the effects of snowfalls, covering the CR provides a viable alternative in areas where the total accumulation is low. Although this leads to a slight drop in the signal response from the CR, the overall quality assessment analysis showed that the ideal IRF was maintained throughout in all images. After the successful installation of the CRs on the HG, we observed good visibility of the CRs in selected images of both PAZ and Sentinel-1 mostly after the initial period of installation. With these images pairs, we estimated velocities for the HG using the technique of complex cross correlation. Average summer velocities of 0.04 m/day was estimated for the glacier front from SAR images. We further validated these results from ground measurements which showed average summer velocities of $\approx$ 0.05 m/day. These results are also in agreement with the theoretical estimates.

However, installation and maintenance of the CRs in such topographies also presents many challenges. The effect of snowfalls can be mitigated to some extent by covering the CRs with a hydrophobic plastic film. But heavy snowfall events still make the CRs completely buried in the snow and reduces the RCS. Even at these elevations, especially in the summer months, we may encounter wet snow which leads to the loss of the signal from the CR. Events of avalanches and snow drift provide further challenges to the sustainability of the CRs in these environments. Heavy winds can also degrade the CR orientation further leading to a loss of signal strength. However, even after considering all the aforementioned challenges, the tests highlight the potential of CRs for monitoring small glaciers in complex topographies.

ACKNOWLEDGEMENTS

The authors thank the Spanish Instituto Nacional de Tecnica Aerospacial (INTA) for the PAZ images (Project AO-001-051). Silvan Leinss was supported by the French ministry of Europe and foreign affairs, within the framework of the 'Make Our Planet Great Again' program for postdoctoral researchers.

REFERENCES

Amitrano, D., Guida, R., Di Martino, G., Iodice, A., 2019. Glacier Monitoring Using Frequency Domain Offset Tracking Applied to Sentinel-1 Images: A Product Performance Comparison. *Remote Sensing*, 11(11). https://www.mdpi.com/2072-4292/11/11/1322.

Benoit, L., Dehecq, A., Pham, H.-T., Vernier, F., Trouvé, E., Moreau, L., Martin, O., Thom, C., Deseilligny, M., Briole, P., 2015. Multi-method monitoring of Glacier d'Argentière dynamics. *Annals of Glaciology*, 56, 118-128.

Cuffey, K. M., Paterson, W. S. B., 2010. *The Physics of Glaciers*. Elsevier Science. OCLC: 761646843.

Eppler, J., Rabus, B. T., 2022. The Effects of Dry Snow on the SAR Impulse Response and Feasibility for Single Channel Snow Water Equivalent Estimation. *IEEE Transactions on Geoscience and Remote Sensing*, 60, 1-23.

Faillettaz, J., Sornette, D., Funk, M., 2011. Numerical modeling of a gravity-driven instability of a cold hanging glacier: reanalysis of the 1895 break-off of Altelsgletscher, Switzerland. *Journal of Glaciology*, 57(205), 817–831.

Gao, J., Liu, Y., 2001. Applications of remote sensing, GIS and GPS in glaciology: a review. 25(4), 520–540. https://doi.org/10.1177/030913330102500404. _eprint: https://doi.org/10.1177/030913330102500404.

Groot, J., Otten, M., 1994. SAR imaging of corner reflectors larger than the spatial resolution. *IEEE transactions on geoscience and remote sensing*, 32(3), 721–724.

Haeberli, W., Schaub, Y., Huggel, C., 2017. Increasing risks related to landslides from degrading permafrost into new lakes in de-glaciating mountain ranges. *Geomorphology*, 293, 405-417. Permafrost and periglacial research from coasts to mountains.

Helfricht, K., Lehning, M., Sailer, R., Kuhn, M., 2015. Local extremes in the lidar-derived snow cover of alpine glaciers. *Geografiska Annaler: Series A, Physical Geography*, 97(4), 721-736. https://doi.org/10.1111/geoa.12111.

Hoelzle, M., Darms, G., Lüthi, M. P., Suter, S., 2011. Evidence of accelerated englacial warming in the Monte Rosa area, Switzerland/Italy. 5(1), 231–243. https://tc.copernicus.org/articles/5/231/2011/.

Huggel, C., Haeberli, W., Kääb, A., Bieri, D., Richardson, S., 2004. An assessment procedure for glacial hazards in the Swiss Alps. 41(6), 1068–1083. http://www.nrcresearchpress.com/doi/10.1139/t04-053.

Jauvin, M., Yan, Y., Trouvé, E., Fruneau, B., Gay, M., Girard, B., 2019. Integration of Corner Reflectors for the Monitoring of Mountain Glacier Areas with Sentinel-1 Time Series. *Remote Sensing*, 11(8). https://www.mdpi.com/2072-4292/11/8/988.

Jóhannesson, T., Arnalds, Þ., 2001. Accidents and economic damage due to snow avalanches and landslides in Iceland. *Jökull*, 50, 81–94.

Maggioni, M., Cola, G., Scotti, R., Freppaz, M., Monti, F., 2018. Ice/snow avalanches from the hanging snout of the palòn de la mare glacier (central italian alps).

Magnin, F., Haeberli, W., Linsbauer, A., Deline, P., Ravanel, L., 2020. Estimating glacier-bed overdeepenings as possible sites of future lakes in the de-glaciating Mont Blanc massif (Western European Alps). *Geomorphology*, 350, 106913.

Margreth, S., Funk, M., Tobler, D., Dalban, P., Meier, L., Lauper, J., 2017. Analysis of the hazard caused by ice avalanches from the hanging glacier on the Eiger west face. *Cold Regions Science and Technology*, 144, 63-72. International Snow Science Workshop 2016 Breckenridge.

Mätzler, C., 1987. Applications of the interaction of microwaves with the natural snow cover. *Remote Sensing Reviews*, 2, 259-387.

Mätzler, C., 1996. Microwave permittivity of dry snow. *IEEE Trans. Geosci. Remote Sens.*, 34(2), 573-581.

Patzelt, G. et al., 1983. Die Berg-und Gletscherstürze vom Huascaran, Cordillera Blanca, Peru. *Hochgebirgsforschung–High Mountain Research*, 6.

Pralong, A., Funk, M., 2006. On the instability of avalanching glaciers. *Journal of Glaciology*, 52(176), 31–48.

Quincey, D. J., Lucas, R. M., Richardson, S. D., Glasser, N. F., Hambrey, M. J., Reynolds, J. M., 2005. Optical remote sensing techniques in high-mountain environments: application to glacial hazards. 29(4), 475–505. https://doi.org/10.1191/0309133305pp456ra.

Raymond, M., Wegmann, M., Funk, M., 2003. Inventory of dangerous glaciers in Switzerland. *Notices from the Research Institute for Hydraulic Engineering, Hydrology and Glaciology at the Swiss Federal Institute of Technology in Zurich*.

Sarabandi, K., Chiu, T.-C., 1996. Optimum corner reflectors for calibration of imaging radars. *Antennas and Propagation, IEEE Transactions on*, 44(10), 1348-1361.

Smith, M. J., Paolo Paron, James S. Griffiths, TotalBoox, TBX, 2011. *Geomorphological Mapping*. Elsevier Science. OCLC: 969051778.